Corrosion Science 257 (2025) 113321

Contents lists available at ScienceDirect

Corrosion Science

journal homepage: www.elsevier.com/locate/corsci

Transpassive-repassivation process of Ni-base superalloys: The role of hidden subsurface alloy layer

Xiaoqi Yue [a,c], Alfred Larsson [b], Dihao Chen [a,c], Andrea Grespi [b], Giuseppe Abbondanza [b], Ulrich Lienert [d], Zoltan Hegedüs [d], Arno Jeromin [e], Thomas F. Keller [e,f], Mattia Scardamaglia [g], Andrey Shavorskiy [g], Chaofang Dong [c], Edvin Lundgren [b], Jinshan Pan [a,*]

[a] KTH Royal Institute of Technology, Division of Surface and Corrosion Science, Stockholm 100 44, Sweden
[b] Lund University, Division of Synchrotron Radiation Research, Lund 221 00, Sweden
[c] University of Science and Technology Beijing, Institute of Advanced Materials and Technology, Beijing 100083, China
[d] DESY Photon Science, Hamburg 22607, Germany
[e] Centre for X-ray and Nano Science (CXNS), Deutsches Elektronen-Synchrotron DESY, Hamburg 22603, Germany
[f] Department of Physics, University of Hamburg, Hamburg 22607, Germany
[g] MAX IV Laboratory, Lund University, Lund 221 00, Sweden

ARTICLE INFO

Keywords:
Ni-base superalloy
Passive film
Subsurface alloy layer
Repassivation
Synchrotron X-ray measurement, DFT calculation

ABSTRACT

Passivity refers to spontaneous formation of a passive film on the surface of metals. High stability of the passive film on advanced alloys relies on the repassivation ability of the alloys in corrosive environments. Two Ni-base superalloys (Ni-22Cr-9Mo-5Fe-2Nb and Ni-18Cr-3Mo-20Fe-5Nb) are studied to elucidate the mechanism of repassivation through a combination of multimodal in-situ synchrotron X-ray measurements, electrochemical measurements, and first principles calculations. The synchrotron X-ray analyses enabled in-situ probing of the passive film and the hidden subsurface alloy layer. The results reveal chemical and structural evolutions of both the passive film and the underlying subsurface alloy layer under transpassive condition. The first principles calculations demonstrate a crucial role of the subsurface alloy layer in the repassivation of the alloys. Upon passivity breakdown at high electrochemical potentials, the passive film rich in Cr oxide becomes highly defective with vacancies, and metal dissolution leads to generation of vacancies (mainly Ni) in the subsurface alloy layer. This promotes repassivation process by enhanced outward Cr diffusion strengthening the metal bond (more Cr-Ni bonds) in the subsurface alloy layer and, together with the enrichment of high valence Mo- and Nb-oxides in the passive film, lead to repassivation when the high potential is removed, which is different from Fe-rich alloys.

1. Introduction

Various metallic materials are widely used in modern society. In many cases, this is possible thanks to “passivity”, i.e., spontaneously formation of a thin passive film on the surface that reduces the corrosion rate to a negligible level [1]. Therefore, passivity is claimed to be the basis of our metal-based civilization [2]. However, passive film breakdown may occur under certain conditions, leading to fast corrosion such as pitting [3]. Stainless steel is a typical example, when stable pitting initiates the broken passive film cannot be self-repaired, so pitting corrosion propagates quickly [4,5]. The stability of the passive film relies on the repassivation ability of the alloy in corrosive environments. Extensive efforts have been made to improve the passive film stability by adding alloying elements and utilizing synergistic effects of alloying elements [6,7]. Although there are different proposed mechanisms of the effects of alloying elements, an atomistic understanding of the repassivation is still not fully understood [8].

Ni-base superalloys contain other metals including Cr, Mo, Fe, and Nb [9], and the passive film is mainly composed of Cr, Mo, Fe, or Nb oxides [10–15]. These alloys exhibit excellent corrosion resistance, strength and heat resistance, making them vital for demanding applications [16]. However, in harsh environments with high chloride

---

* Corresponding author.
E-mail address: jinshanp@kth.se (J. Pan).

https://doi.org/10.1016/j.corsci.2025.113321
Received 2 June 2025; Received in revised form 12 September 2025; Accepted 15 September 2025

concentration and low pH, there is a high risk of depassivation as reflected in the recommended applications of Ni-base superalloys. The best strategy to avoid severe localized corrosion after such a breakdown is a strong ability of repassivation [17]. Ni-base superalloys show a different passivity breakdown behavior compared to Fe-based stainless steel [4,18,19]. Recently, we reported a transpassive breakdown mode for Ni–Cr–Mo alloys driven by Oxygen Evolution Reaction (OER), which is different from the classical model of transpassive breakdown of stainless steel where Cr^{3+} is oxidized to soluble Cr^{6+}; instead, the Mo^{4+} oxide in the passive film is further oxidized into Mo^{6+} complexes, in parallel to OER and dissolution mainly of Ni [14,20–23].

Depassivation occurs via dissolution or rupture of the barrier layer due to different reasons e.g., high over potential, high halide content, and high temperature [24]. Repassivation can be achieved when a thin layer of oxide forms at the interface between the metal and the hydrous metal halide [18], showing a hysteresis loop in the polarization curve [25–27]. Unlike stainless steel, the current density for Ni-base superalloys is often suppressed immediately when the applied potential is decreased, without considerable hysteresis loop [28,29]. The alloying elements affect the repassivation tendency, especially Cr, which facilities the oxide reformation [30,31]. For designing high-performance alloys, it is needed to clarify how the chemistry and structure of the interfacial region (metal-oxide-electrolyte) evolve under transpassive condition and how that correlates with the suppression of metal dissolution leading to repassivation. Detailed information about the processes occurring within both the oxide film and the subsurface alloy layer under transpassive condition is crucial for fundamental understanding of the mechanism of repassivation for Ni-base superalloys.

In this work, two commercial Ni-base superalloys (Ni-22Cr-9Mo-5Fe-2Nb and Ni-18Cr-3Mo-20Fe-5Nb, composition giving in Table 1 and Table 2), one with lower Fe-content and higher Cr- and Mo-contents, and another with higher Fe-content and lower Cr- and Mo-content, were chosen for the study of mechanism of transpassive breakdown and repassivation. Utilizing multimodal in-situ synchrotron-based X-ray techniques combined with electrochemical measurements, we have investigated the changes of the passive film and the subsurface alloy layer during a stepwise increase of the applied potential up to transpassive breakdown region, and then stepwise decrease of the potential back to the passive region. X-ray Reflectivity (XRR) and Ambient-Pressure X-ray Photoelectron Spectroscopy (APXPS) were used to investigate the chemical and structural degradation of the surface film and the concurrent changes in the subsurface alloy layer. X-ray Fluorescence (XRF) was used to quantify the metal dissolution during depassivation and repassivation. Grazing-Incidence X-ray Diffraction (GI-XRD) was used to determine the lattice changes in the subsurface alloy layer. These in-situ synchrotron X-ray analyses provide unprecedented information of the changes in the subsurface alloy layer. Moreover, complementary first-principles modelling was carried out to investigate the lattice change, metal bonding, and ionic transport in the near surface region. Combining these unique results allowed us to elucidate the atomistic mechanism of repassivation on the basis of the real-time monitoring of passive film degradation, metal dissolution, and structural evolution of the subsurface alloy layer.

2. Material and methods

2.1. Preparation of the samples

Two commercial Ni-base superalloys, UNS N06625 and N07718, purchased from VDM Metals, were used in this study. The two alloys have high a Cr content and contain a few percent of Nb. Ni-22Cr-9Mo-5Fe-2Nb (identified as N06625) has a low Fe-content and high Mo-content, while Ni-18Cr-3Mo-20Fe-5Nb (identified as N07718) has a high Fe-content and low Mo-content. Detailed chemical composition of the alloys can be found in Table 1 and Table 2. The materials (in standard annealed condition) were cut into samples with a radius of 6 mm and a thickness of 3 mm. The samples were mirror polished by mechanical polishing, followed by electrochemical polishing to release the residual stress induced by mechanical polishing (micrometer scale in the surface layer), and then cleaned by sonication in acetone, ethanol, and deionized water for 5 min, respectively. Finally, the samples were dried with N_2 and separately stored in desiccators for surface protection prior to experiments.

2.2. Electrochemical measurements

Cyclic polarization curves were measured at room temperature by using an electrochemical workstation (GAMRY Reference 600 +) and a three-electrode system, with the sample as the working electrode, Pt wire as the counter electrode, and the saturated Ag/AgCl electrode as the reference electrode. The sample was mounted in PEEK fixture. A conductive screw was used to tighten the back of the sample and eliminate the crevice between the sealing ring and the sample. Before the polarization measurement, the open circuit potential (OCP) was recorded for 30 min. Cyclic polarization curves were obtained from −200 mV vs. OCP with an apex potential of 1.3 V vs. Ag/AgCl and a scan rate of $0.167\ mV\ s^{-1}$.

In-house electrochemical potential step measurements with the same electrode system were carried out in the same loop sequence as in the synchrotron measurements, which was done by using a portable potentiostat (Autolab PGSTAT204). Each loop included 3 sequences: *i)* potentiostatic measurement at an applied potential to reach a steady state (10 min); *ii)* electrochemical impedance spectroscopy (EIS) at the applied potential (15 min); *iii)* synchrotron measurements at the applied potential (30 min). The potential steps included the OCP, upward scans at 0.4 V, 0.6 V, 0.8 V, 0.9 V, 1 V, 1.1 V, 1.2 V, 1.3 V and downward scans at 1.2 V, 1.1 V, 1.0 V, 0.9 V, 0.8 V vs. Ag/AgCl. The EIS was measured at an AC amplitude of 5 mV, with a frequency range from 100 kHz to 0.01 Hz in the potential range from OCP to 0.8 V, but to 0.1 Hz when the potential was above 0.8 V vs. Ag/AgCl.

Additionally, Mott-Schottky plots were measured after forming a stable film by potentiostatic polarization for 1800 s at 0.6 V in the passive region and 0.9 V in the transpassive region, then measuring the capacitance from the formation potential down to cathodic region with a scan rate of 50 mV/s at 1000 Hz.

The electrolyte was 1 M and 0.1 M NaCl solutions, which were prepared using Milli-Q water. The 1 M NaCl solution was degassed using N_2 before and during the experiments. The solution was refreshed after the end of each loop for all potential steps. The 0.1 M NaCl solution was prepared and pre-vacuum degassed for the APXPS measurement to avoid rapid evaporation of the electrolyte due to continuous pumping of the vacuum chamber. The EIS measurement in the loop was skipped for

Table 1
The main composition (wt%) of the two Ni-Cr-Mo-Fe-Nb alloys.

	UNS No	*Ni*	*Cr*	*Mo*	*Fe*	*Nb*
Ni−22Cr−9Mo−5Fe−2Nb	N06625	61.53*	21.53	8.63	4.38	3.32
Ni−18Cr−3Mo−20Fe−5Nb	N07718	52.28	18.34	2.91	19.50*	5.10

* Balanced value

Table 2
Composition (wt%) of other minor alloying elements in Ni-Cr-Mo-Fe-Nb alloys.

	UNS No	*Ti*	*Al*	*C*	*Si*	*Mn*	*P*	*S*
Ni−22Cr−9Mo−5Fe−2Nb	N06625	1	0.5	0.02	0.12	0.05	< 0.015	< 0.001
Ni−18Cr−3Mo−20Fe−5Nb	N07718	-	-	0.05	0.07	0.07	< 0.015	< 0.001

testing in 0.1 M NaCl solution. All electrochemical tests were performed at room temperature.

2.3. *In-situ synchrotron surface and interface characterizations*

The Swedish Material Science beamline P21.2 at PETRA III in DESY, Hamburg, Germany, was used to perform in-situ GI-XRD, XRR, and XRF measurements. The experimental setup has been described previously [20]. The beam size was 50 × 500 ($V \times H$) μm^2 and the X-ray energy was 38 keV. In the XRR measurement [11,20], a Cyberstar X2000 scintillator was used on a motorized stage changing the angle from 0.02 to 3°. Analysis of the measured XRR data was done using GenX. GI-XRD was measured at an incidence angle of 0.3° using a VAREX flat panel detector. A CeO_2 sample was used to calibrate the detector distance and position. By integrating GI-XRD data using PyFAI, the lattice parameter of the surface region at each potential step was extracted through Le Bail refinements using GSAS-II software. XRF measurements were conducted using an Amptek FAST SDD silicon drift detector, which was mounted perpendicularly to the X-ray beam and positioned 10 cm away from the incoming X-ray beam. An acquisition time of 60 s was used to detect the fluorescence signals from the dissolved metal ions in the electrolyte. The energy scale was calibrated using fluorescence of Cu, Rb, Mo, and Ag excited by a radioactive Am source. The XRF intensities were calibrated using a series of reference solutions of known concentrations (0.1 M, 0.01 M, and 0.001 M) of Ni, Cr, Fe, and Mo salts. The in-situ GI-XRD, XRR, and XRF measurements were conducted at step III under each applied potential using a special electrochemical cell designed for synchrotron measurements. The wall thickness of the electrochemical cell above the sample is very thin so that the X-ray beam can easily pass through, which allows in-situ measurement under electrochemical operation. The cell has been described in detail in our previous paper [20].

The in-situ APXPS measurements were performed at the HIPPIE beamline at MAX IV, Lund, Sweden [32,33]. An excitation energy of 1600 eV, pass energy of 200 eV, energy step of 0.15 eV, slit of 30 μm, and a beam size of 25 × 60 ($V \times H$) μm^2 were used for all core levels, and the measurement was done at ambient pressure of 17 mbar (equal to the electrolyte's vapor pressure). Three electrode system was mounted on a manipulator, which could then be lifted and immersed into a glass beaker placed in the vacuum chamber. The sample was immersed into solution to reach a steady state (step I), then lifted out to approach the analyzer for APXPS measurements with a thin electrolyte layer (~ 20 nm) covering the surface (sequence *iii*). No external voltage was applied in this step for APXPS measurements. For the XPS spectra fitting, an asymmetric Voigt line shape [34] was used to fit the metal components of the Ni 2p, Cr 2p, and Mo 3d core levels, which all display asymmetry toward higher binding energy. All other peaks were fitted using Voigt line profiles. All spectra were background-subtracted using a Shirley background. The fitted AP-XPS spectra, fitting parameters, and details of the quantitative analysis are given in the Supporting Information. Further details can be found in earlier works [10,11,20,33,35].

2.4. *Ex situ surface characterizations*

The surface morphology after the electrochemical measurements were examined using a high-resolution field emission SEM (Nova Nano SEM 450, FEI Thermofisher) with an acceleration voltage of 5 keV. The chemical composition was analyzed by an X-Max 150 EDS silicon drift detector (Oxford) with an acceleration voltage of 10 keV [36].

2.5. *Theoretical computation details*

The spin-polarized density functional theory (DFT) calculations [37] were performed in Vienna ab initio simulation package (VASP). The generalized gradient approximation (GGA) of the Perdew-Burke-Ernzerhof (PBE) functional was used to describe the exchange-correlation potential [38]. The cutoff energy of plane-wave was set to 450 eV for all calculations, and the convergence criterion for the energy was 10^{-5} eV. The Brillouin zone was sampled by the Monkhorst-Pack mesh [39]. The structural relaxations were conducted until the forces on all the relaxed atoms were less than 0.01 eV/Å.

For Cr_2O_3, the GGA+U method was applied to correct the on-site Coulomb interactions of d-orbital electrons, and Hubbard U corrections with $U_{eff} = 5.5$ eV were applied for Cr. The diffusion energy barrier was calculated by transition state theory using the climbing image nudged elastic band (CINEB) method [40]. The convergence criterion for the forces on all atoms was 0.03 eV/Å. The in-plane magnetic order of Cr atoms was ferromagnetic, and the interlayer antiferromagnetic order of Cr atom layers along [0001] was adopted the order of $+ - + -$ [41].

3. Results and discussion

3.1. *Transpassive breakdown and repassivation on the Ni-base alloys*

Electrochemical results in Fig. 1a show transpassive breakdown of the two alloys at potentials above 0.75 V, i.e., significantly increased current density with increased potential. Upon reversing the potential scan at 1.35 V, the current density of Ni-22Cr-9Mo-5Fe-2Nb (low Fe-content) decreased sharply in the downward potential scan (Fig. 1b), and the absence of a considerable hysteresis loop indicates efficient repassivation. For Ni-18Cr-3Mo-20Fe-5Nb (high Fe-content), however, the current density remained high within the high potential region in the downward scan, indicating a delayed repassivation (Fig. 1c). A higher Cl^- concentration results in easier degradation for both two alloys, however, Ni-22Cr-9Mo-5Fe-2Nb is less sensitive to Cl^- concentration, indicating it's a higher ability for repassivation. Thus, the results and discussion are more focused on this low Fe-content alloy, while part of results of the high Fe-content alloy are given in Supplementary Notes.

Mott-Schottky plot analysis was done for the passive film formed in the passive condition (0.6 V) and transpassive condition (0.9 V), respectively. The plots and calculated point defect (acceptor, N_A) density are show in Fig. 1d, which confirms that the passive film becomes highly defective (high N_A) under transpassive condition. The EIS measurements were also performed, showing that total resistance decreases with increase of applied potential. The details of the Mott-Schottky plot and EIS results and the calculations can be found in Supplementary Note 1.

3.2. *Evolution of the passive film and the subsurface alloy layer during breakdown*

Figs. 2a-2e show the APXPS spectra of Ni $2p_{3/2}$, Cr $2p_{3/2}$, Mo 3d, Nb 3d, and Fe $2p_{3/2}$ core levels measured for Ni-22Cr-9Mo-5Fe-2Nb with the presence of a thin electrolyte layer on the surface (i.e., in-situ). All the spectra were background-subtracted using the Shirley curve. The binding energy (BE) was calibrated by the Ni metallic peak at 582.8 eV. The experimental data are plotted as solid lines; the cumulative fits are shown as dot lines (matching well the experimental data). The passive

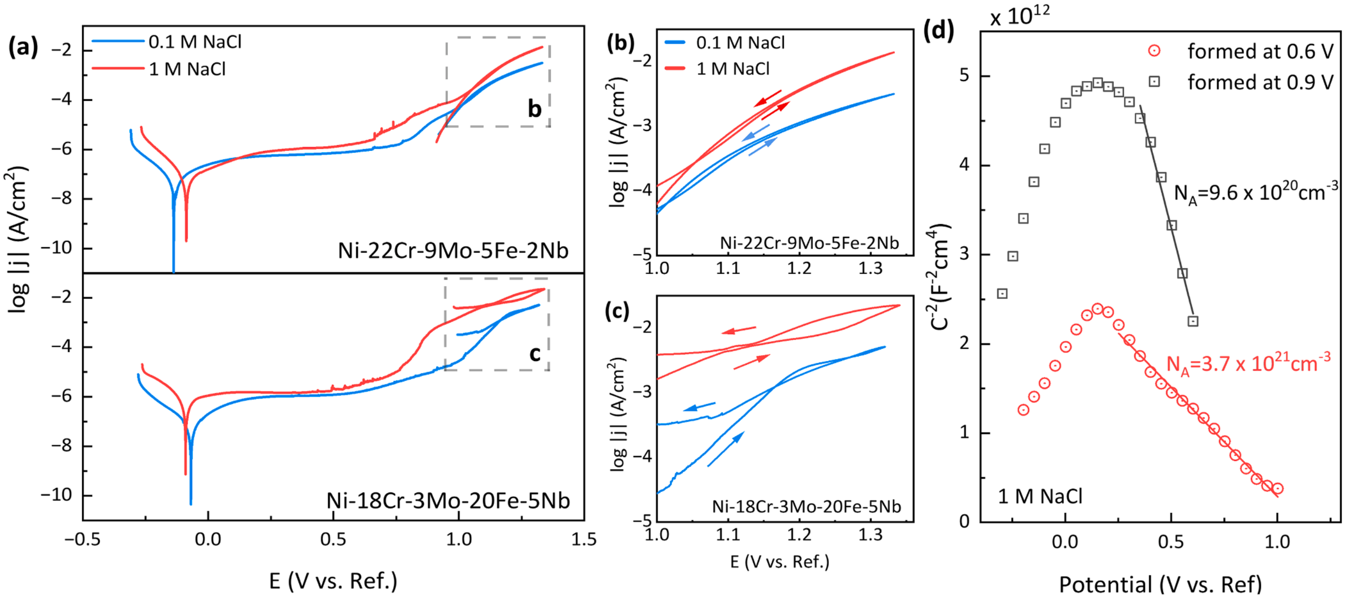

Fig. 1. (a) Cyclic polarization curves of the two Ni-base superalloys at a scan rate of 0.167 mV s^{-1}. (b)-(c) Enlarged diagram showing repassivation trends. (d) Mott-Schottky plots of the passive films on Ni-22Cr-9Mo-5Fe-2Nb in 1 M NaCl solution.

film is enriched in Cr_2O_3 (green-marked in Fig. 2b) at OCP and in passive state, while Fe-components are minor. The proportion for Fe-, Ni-, Mo- and Nb-compounds increase with increasing potential. The proportion for Cr- and Ni-hydroxides and Mo^{6+} and Nb^{5+} compounds (purple-marked) increase with increasing potential. At 0.9 V, the APXPS signals of metallic components (blue-marked) are greatly attenuated by a thick surface film, and the signals from the oxides are dominated by the high-valence Mo^{6+} and Nb^{5+} compounds, indicating their enrichment in the passive film under higher anodic potentials. The composition of the passive film formed on Ni-base alloys has been studied extensively and become well-known in recent years, so in this study the analysis has been focused on the subsurface alloy layer, which is basically unknown. From the detectable metallic signals (Figs. 2a-2e), the composition of the passive film and the subsurface alloy layer beneath the passive film was calculated, as shown in Figs. 2f and 2g. Detailed data analysis can be found in Supplementary Note 2. These results show the evolution of both the passive film and the subsurface alloy layer with increasing applied anodic potential. The pronounced changes of the passive film and subsurface alloy layer coincide with the onset of OER, which generates higher concentration of H^+ as shown in Reaction (1) [20]:

$$2H_2O \leftrightarrow O_2 + 4H^+ + \quad 4e^- \qquad (1)$$

The high-valence Mo^{6+} and Nb^{5+} compounds remain thermodynamically stable in the acidified environment induced by OER, as shown in the Pourbaix diagram in Supplementary Note 2. $MoO_3 \cdot H_2O$ remains stable above pH 4, while NbO_2OH is stable below pH 1.

Such changes were also observed on Ni-18Cr-3Mo-20Fe-5Nb (Fig. 3), which exhibits the depressed OER (less O_2 bubble forming). The depressed OER phenomenon coincides with variation in surface evolution. The metallic peaks of Ni, Cr, Mo and Fe are clearly detectable at 900 mV, indicating a thin passive film on the surface. After polarization at 1400 mV, these metallic peaks are also detected, and the hydroxide peaks are pronounced in the spectra (Fig. 3). These observations suggest that no thick passive film is formed during transpassive breakdown of Ni-18Cr-3Mo-20Fe-5Nb, which is different from Ni-22Cr-9Mo-5Fe-2Nb. The reason is probably related to the lower Mo content in Ni-18Cr-3Mo-20Fe-5Nb compared to Ni-22Cr-9Mo-5Fe-2Nb, consistent with the catalytic cycle of OER by forming Mo^{6+} mentioned in previous literature [20]. Therefore, the transpassivity of Ni-18Cr-3Mo-20Fe-5Nb with higher Fe and Nb are less affected by the OER, which will be discussed in more detail later.

Fig. 4 shows the thickness and density of the passive film and the subsurface alloy layer of Ni-22Cr-9Mo-5Fe-2Nb obtained from in-situ XRR measurement, which was stopped after the potential step at 0.9 V because the surface became rough. The density of the passive film decreased by ca. 30 % up to 0.9 V (Fig. 4b), indicating degradation of the passive film towards the passivity breakdown. For comparison, fitted XRR data for Ni-18Cr-3Mo-20Fe-5Nb and the values of thickness and density for surface film and surface alloy layer are shown in Fig. 5. The density of the passive film decreased by ca. 20 % up to 1.3 V for Ni-18Cr-3Mo-20Fe-5Nb (Fig. 5c).

The ionic transport in the oxide layer is affected by the density of the oxide. The vacancy density (N_A) of the defective passive film formed at 0.9 V is 4 times of that of the protective passive film formed at 0.6 V (Fig. 1d). As shown in the upper part of Fig. 6, the diffusion energy barrier for Cr diffusion through the cation vacancy in Cr_2O_3 layer was calculated. This energy barrier decreases from 4.14 to 2.14 eV as the defect density increases from 8.6×10^{20} cm^{-3} (passive condition, Figs. 6a) to 3.4×10^{21} cm^{-3} (transpassive condition, Fig. 6b), which indicates a significantly weaker barrier of the detective passive film against metal dissolution. Under transpassive condition above 0.9 V, the enhanced metal dissolution results in higher defect densities of the passive film. This leads to multiple pathways for ion diffusion through vacancies with a lower energy barrier. The presence of vacancies nearby could further decrease the diffusion energy barrier through the defective passive film. The Cr diffusion energy barrier through the Cr_2O_3 layer further decreases to 1.809 eV as the defect density reaches 1×10^{22} cm^{-3}, as shown in Fig. 6c. Note that the diffusion of ions via interstitial sites is also promoted by a higher density of vacancies. The lower part of Fig. 6 presents the DFT-computed Cr diffusion energy barrier for alternative ionic transport path in the passive film via interstitial sites in Cr_2O_3 layer and corresponding interstitial paths (Figs. 6d-6f), showing the changes from defect-free (Fig. 6d) to highly defective layer with the defect density of 3.4×10^{21} cm^{-3} (Figs. 6e) and 1.0×10^{22} cm^{-3} (transpassive condition, Fig. 6f), respectively. These DFT calculations prove that the diffusion energy barriers of Cr diffusion through vacancy and interstitial sites decrease as the cation vacancy density of the passive film increases. More detailed DFT calculations of ionic transport (Cr diffusion) in the passive film can be found in Supplementary Note 3. Therefore, under transpassive condition, the highly defective passive

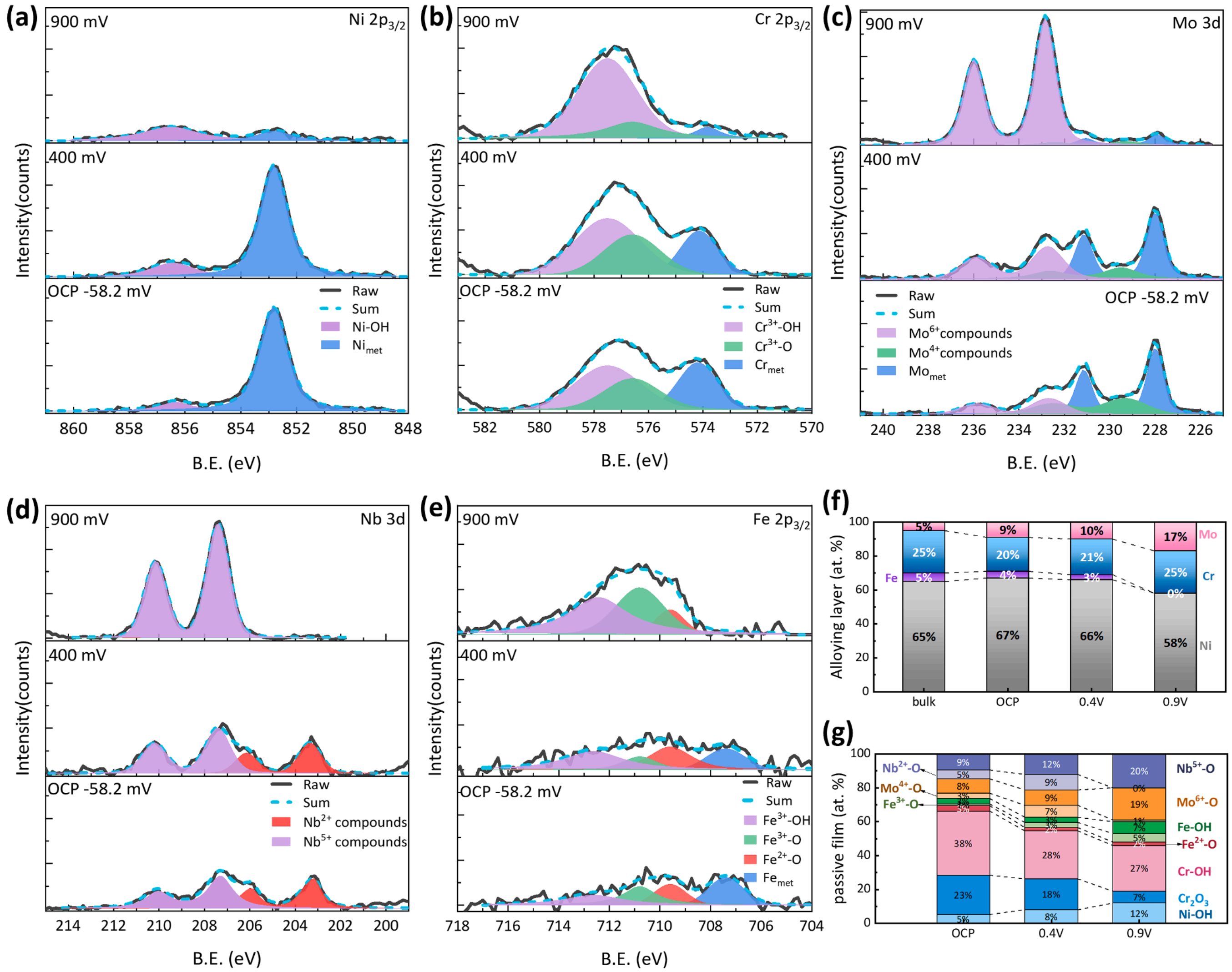

Fig. 2. APXPS spectra of (a) Ni 2p3/2, (b) Cr 2p3/2, (c) Mo 3d, (d) Nb 3d, and (e) Fe $2p_{3/2}$, respectively, for Ni-22Cr-9Mo-5Fe-2Nb in 0.1 M NaCl versus applied potential. Composition (at%) of the (f) subsurface alloy layer and (g) passive film of Ni-22Cr-9Mo-5Fe-2Nb, calculated from the APXPS data.

film does not act as an effective barrier against metal dissolution.

The density of the subsurface alloy layer of Ni-22Cr-9Mo-5Fe-2Nb increased slightly with potential up to 0.8 V, but sharply decreased as the applied potential increased to 0.9 V (Fig. 4b), indicating formation of vacancies due to enhanced metal dissolution. As seen in Fig. 2f, in the subsurface alloy layer, metallic Nb is not detectable, and the percentage of Mo increased while Fe decreased as the applied potential increased in the passive region. This is consistent with the gradual increase of density since Mo atom is heavier than Ni, Fe and Cr. The depletion of Nb in the subsurface alloy layer can be explained by its highest oxidation tendency (lowest standard electrode potential, Nb<Cr<Fe<Ni<Mo), leading to its preferential oxide formation. Lower percentage of Cr and Fe in the subsurface alloy layer compared to the bulk composition can also be attributed to their oxidation to form surface oxide. When the potential was increased up to 0.9 V, Mo became significantly enriched and Fe became negligible, while the percentage of Ni decreased by 8 % in the subsurface alloy layer. This is in line with the observation that the density of the subsurface alloy layer decreased 12.5 % according to the XRR data. The influence of dissolution of Fe and oxidation of Nb on the density of the subsurface layer is likely negligible due to their low contents in the alloy. These results indicate the generation of vacancies due to the enhanced metal (mainly Ni) dissolution at 0.9 V. The higher Cr percentage in the subsurface alloy layer at 0.9 V is due to less Cr dissolution compared to Ni. The Cr becomes further enriched due to enhanced Ni dissolution, see the section below.

3.3. *Metal dissolution from Ni-base superalloys during transpassive breakdown*

Anodic dissolution of Ni, Cr, Mo, and Fe from the two Ni-base superalloys at stepwise increased potentials, followed by stepwise decreased potentials, were measured by XRF. Details of the quantification of the metal dissolution can be found in Supplementary Note 4. As shown in Fig. 7a, enhanced Ni dissolution was detected at and above 1 V for both alloys, which is consistent with the onset of passive film degradation. Meanwhile, Cr dissolution occurred at a low rate, which is higher for Ni-18Cr-3Mo-20Fe-5Nb than Ni-22Cr-9Mo-5Fe-2Nb. Mo dissolution was also detected at a low level, which is higher for Ni-18Cr-3Mo-20Fe-5Nb (52 ng/(cm^{2}s)) than Ni-22Cr-9Mo-5Fe-2Nb (45 ng/(cm^{2}s)) at 1.3 V despite of a lower Mo content in Ni-18Cr-3Mo-20Fe-5Nb. However, no considerable Nb dissolution was detected at all applied potentials. These results suggest that the Mo-oxides are more stable on Ni-22Cr-9Mo-5Fe-2Nb than on Ni-18Cr-3Mo-20Fe-5Nb at the high potentials, while Nb forms stable oxide (like Nb_2O_5) and mostly remains in the passive film.

For Ni-22Cr-9Mo-5Fe-2Nb, the base metal Ni showed the highest dissolution rate, reaching 950 ng cm^{-2}s^{-1} at 1.3 V, while the Cr dissolution rate was much lower, reaching 124 ng cm^{-2}s^{-1} at 1.3 V. The

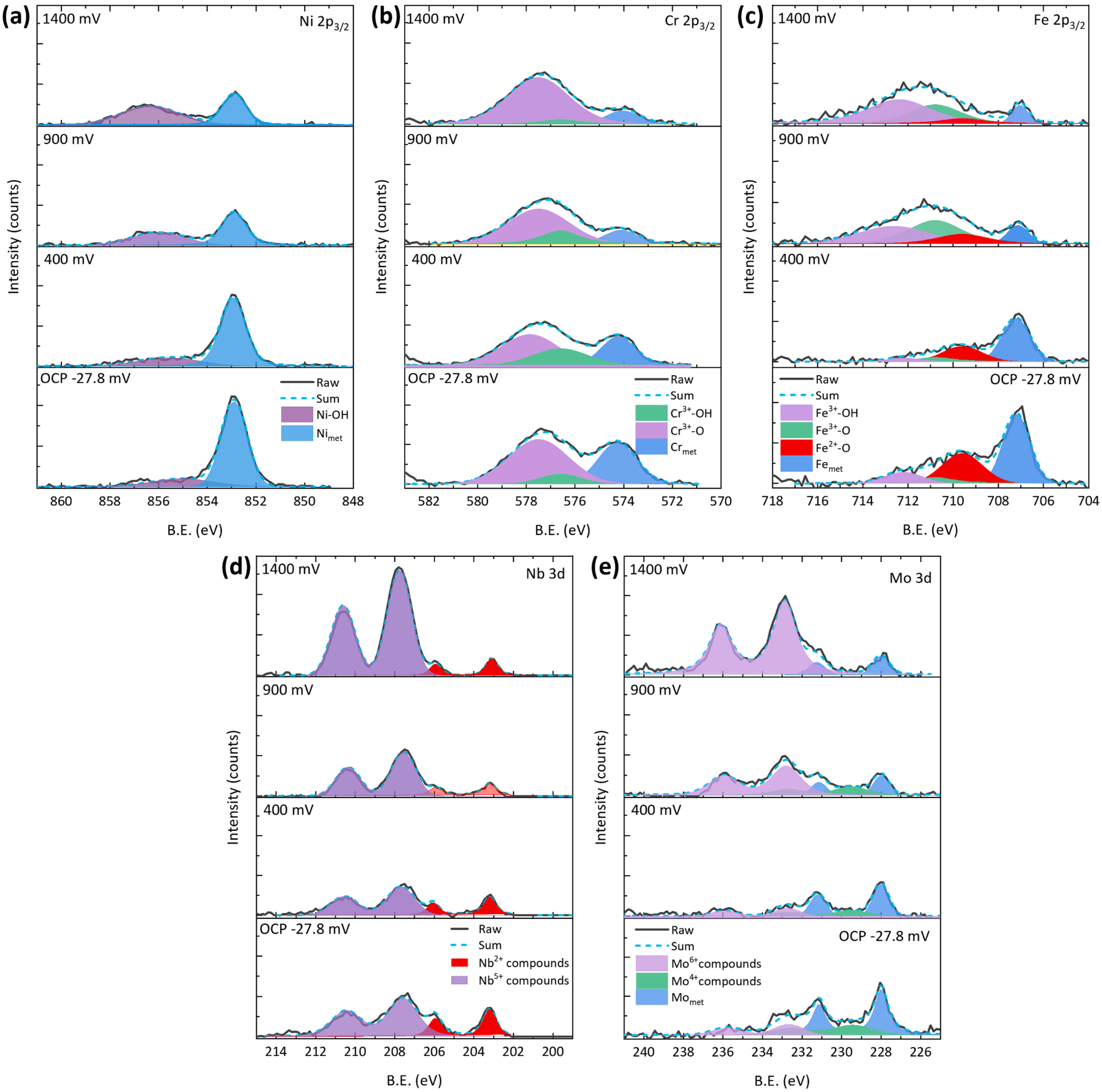

Fig. 3. APXPS spectra of (a) Ni 2p3/2, (b) Cr 2p3/2, (c) Fe $2p_{3/2}$, (d) Nb 3d, and (e) Mo 3d, respectively, for Ni-18Cr-3Mo-20Fe-5Nb in 0.1 M NaCl versus applied potential.

dissolution rate for Mo and Fe was negligible (< 10 ng $cm^{-2}s^{-1}$). Remarkably, for this alloy, the enhanced Ni dissolution with increasing potential did not cause irreversible propagation, since the dissolution rates were similar in the upward and downward potential steps (Fig. 7b), indicating an efficient repassivation.

In contrast, Ni-18Cr-3Mo-20Fe-5Nb showed a lower Ni dissolution rate (500 ng $cm^{-2}s^{-1}$) but a relatively higher Fe dissolution rate (170 ng $cm^{-2}s^{-1}$ at 1.3 V). After the largely enhanced dissolution of Ni (2050 ng $cm^{-2}s^{-1}$) and Fe (997 ng $cm^{-2}s^{-1}$) at 1.4 V, the dissolution rates of Fe, Cr, and Mo further increased although the applied potential was decreased back to 1.3 V. Therefore, the dissolution rate plot of the alloying elements shows pronounced hysteresis loops between upward and downward potential steps (Fig. 7a), which suggests irreversible changes of the subsurface alloy layer due to the passivity breakdown. As shown in Fig. 7b, the total current density of Ni-22Cr-9Mo-5Fe-2Nb is lower than Ni-18Cr-3Mo-20Fe-5Nb after passivity breakdown. Only half of the current for Ni-22Cr-9Mo-5Fe-2Nb is originated from metal dissolution (mainly Ni); while OER accounts for a significant portion of the current, as demonstrated in previous studies on Ni and Ni-Cr-Mo alloy [20,27,42]. However, for Ni-18Cr-3Mo-20Fe-5Nb with a higher Fe-content and lower Cr- and Mo-contents, the total current is mainly attributed to the Ni and Fe dissolution, during the upward and downward steps.

Figs. 7c and 7d show SEM images of the sample surface after the entire measurement sequence for Ni-22Cr-9Mo-5Fe-2Nb and Ni-18Cr-3Mo-20Fe-5Nb, respectively. Loose and dehydrated corrosion products (gel-like in the solution) were observed on the surface, which are Nb^{5+}- and Mo^{6+}-rich compounds, as confirmed by the EDS results

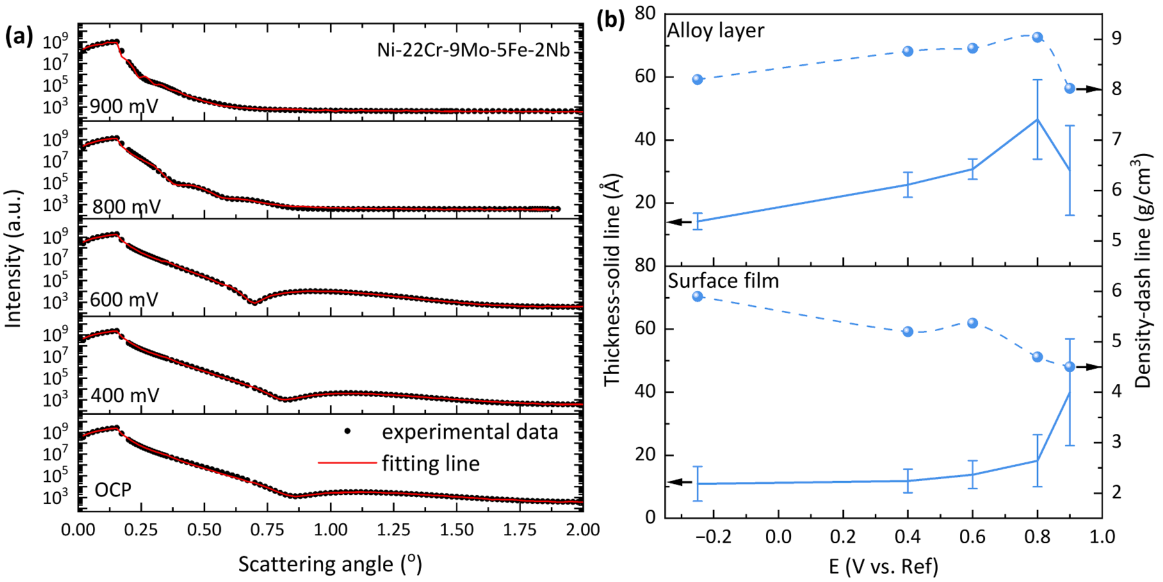

Fig. 4. (a) XRR spectra for Ni-22Cr-9Mo-5Fe-2Nb in 1 M NaCl versus applied potential. (b) Evolution of thickness and density of the passive film and the subsurface alloy layer on Ni-22Cr-9Mo-5Fe-2Nb in 1 M NaCl measured by XRR.

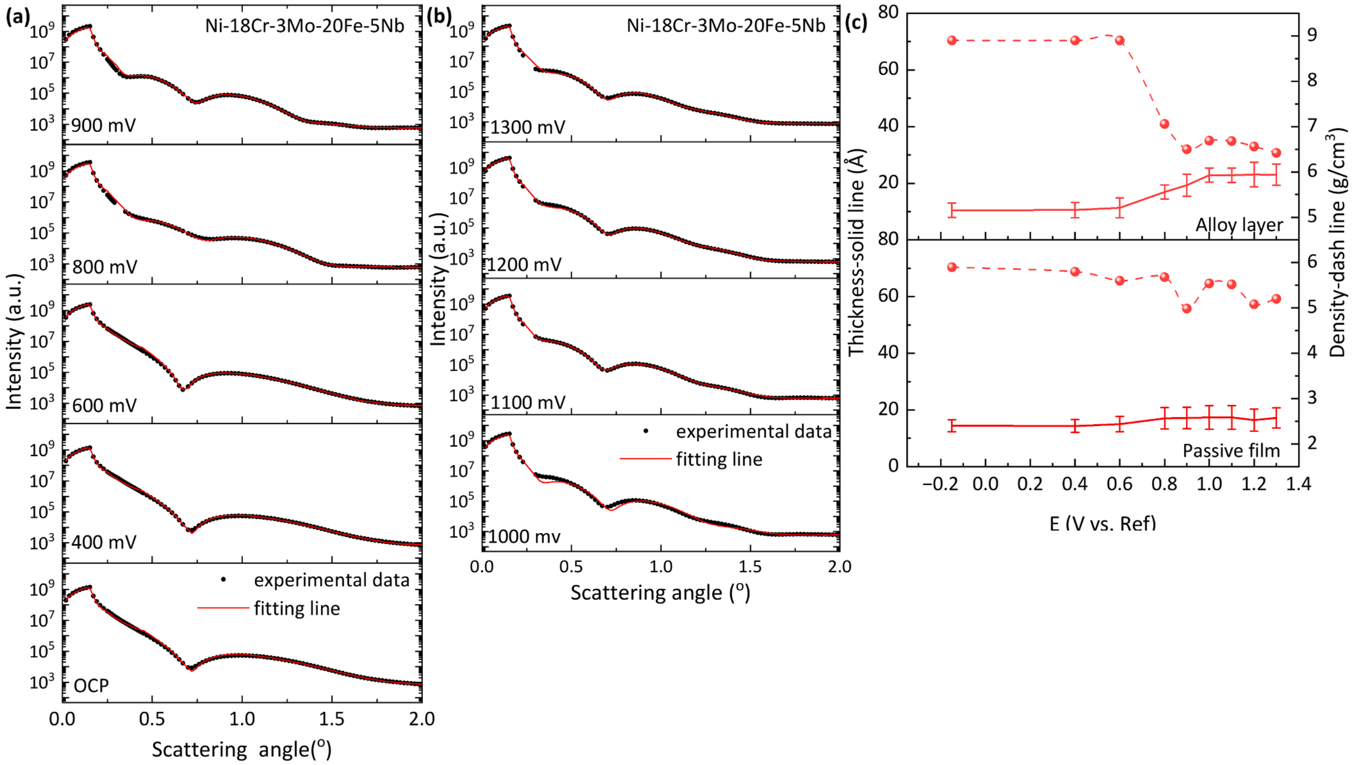

Fig. 5. XRR spectra for Ni-18Cr-3Mo-20Fe-5Nb in 1 M NaCl in (a) passive and (b) transpassive region. (c) Evolution of thickness and density of the passive film and the subsurface alloy layer on Ni-18Cr-3Mo-20Fe-5Nb in 1 M NaCl measured by XRR.

(Supplementary Note 5). The dissolved metal ions come from the passive film and the subsurface alloy layer, and possibly also from the precipitated corrosion products via a chemical reaction. However, the XRF did not detect all dissolved cations (e.g., Nb) since part of them form corrosion products sticking on the surface. This part of the dissolution was detected with a delay until the corrosion products are also dissolving, which explains why the dissolution current calculated from XRF data for Ni-18Cr-3Mo-20Fe-5Nb is larger than the measured total current during the downward steps. It should be noted that the formation of this micron-scale Nb^{5+}- and Mo^{6+}-rich film is associated with the loss of XPS (nanoscale sensitivity) and XRR (nanoscale roughness requirement) signals. Therefore, it can be inferred that the Nb^{5+}- and Mo^{6+}-rich corrosion product film on the Ni-22Cr-9Mo-5Fe-2Nb grows after 0.9 V; while the product film on the Ni-18Cr-3Mo-20Fe-5Nb grows after 1.4 V. The corroded surfaces beneath the mud-cracking corrosion products of the two alloys show different morphologies, i.e., a flat surface for Ni-22Cr-9Mo-5Fe-2Nb (Fig. 7c and Supplementary Note 5) but a cratered surface for Ni-18Cr-3Mo-20Fe-5Nb (Fig. 7d and Supplementary Note 5).

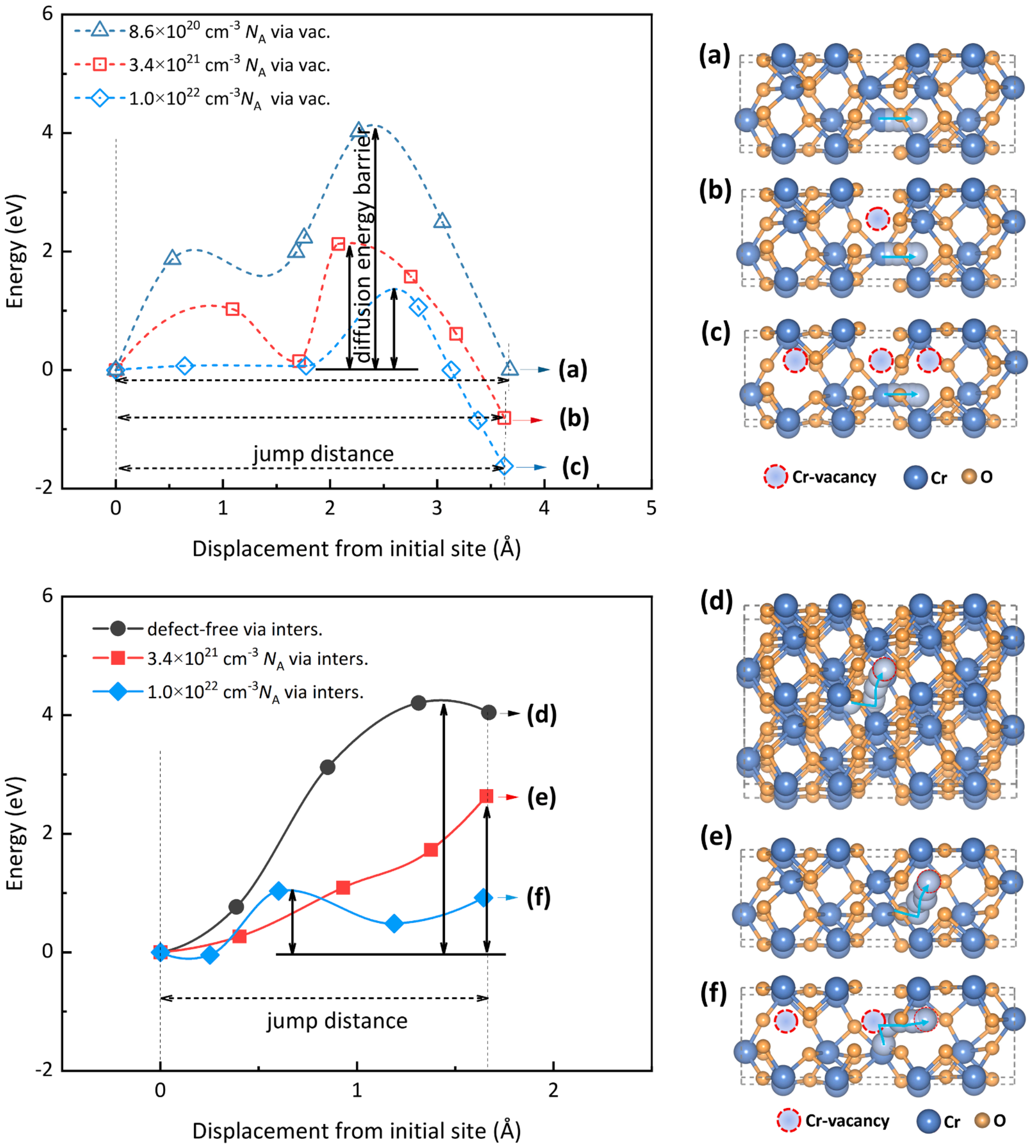

Fig. 6. DFT calculation results of ionic transport (Cr diffusion) through metal vacancy in Cr_2O_3 layer. Curves a-c in the left figure present the DFT calculated energy for the corresponding path for Cr diffusion via Cr-vacancy in passive state (model **a**: defect density 8.6 $\times 10^{20}$ cm^{-3}) and transpassive state (model **b**: 3.4 $\times 10^{21}$ cm^{-3} and model **c**: 1.0 $\times 10^{22}$ cm^{-3}), respectively. Curves d-f in the left figure present the DFT calculated energy for the corresponding path for Cr diffusion via interstitial sites in passive state (model **d**: defect free) and transpassive state (model **e**: 3.4 $\times 10^{21}$ cm^{-3} and model **f**: 1.0 $\times 10^{22}$ cm^{-3}), respectively.

Clearly, Ni-22Cr-9Mo-5Fe-2Nb, with a low Fe-content, has a strong repassivation ability. When the applied potential is decreased, the ‘transpassive-repassivation’ process of Ni-22Cr-9Mo-5Fe-2Nb takes place within the high potential range with a highly defective passive film. This indicates that the subsurface alloy layer plays an important role in the repassivation.

3.4. Repassivation of Ni-base superalloys

The combined results show different repassivation abilities for the two alloys. Ni-22Cr-9Mo-5Fe-2Nb demonstrates the ability for efficient repassivation, whereas Ni-18Cr-3Mo-20Fe-5Nb, with a high Fe-content, shows a weak tendency for repassivation. Repassivation requires that *i*) dissolution of the passive film and the subsurface alloy layer does not lead to irreversible corrosion propagation, and *ii*) reformation of a protective passive film. When transpassive breakdown occurs, the passive film is a highly defective (p-type oxide), which plays a minor role in repassivation. The precipitation of the corrosion products indicates the supersaturation of metal ions in the electrolyte, which confirms the enhanced anodic dissolution from the subsurface alloy layer at the high potentials.

The composition of the subsurface alloy layer differs from the bulk material due to the following reactions occurring at the metal-oxide interface:

$$M \leftrightarrow M_0^{\chi+} + \chi e^- + V_M \tag{2}$$

$$V_M + m \leftrightarrow M + V_m \tag{3}$$

Herein, M, $M_0^{\chi+}$, and V_M represent the metal atom, metal ion, and metal vacancy in the subsurface alloy layer; the reaction (2) indicates the dissolution from the subsurface alloy layer. m and V_m represent the metal atom and metal vacancy in the matrix, and reaction (3) indicates the movement of the metal atom from matrix to the subsurface alloy layer.

In the passive condition, the passive film restrains the anodic dissolution process so the two reactions occur at the same rate, which is very low. Preferential oxidation of certain alloying elements leads to a different composition and thus density of the subsurface alloy layer than

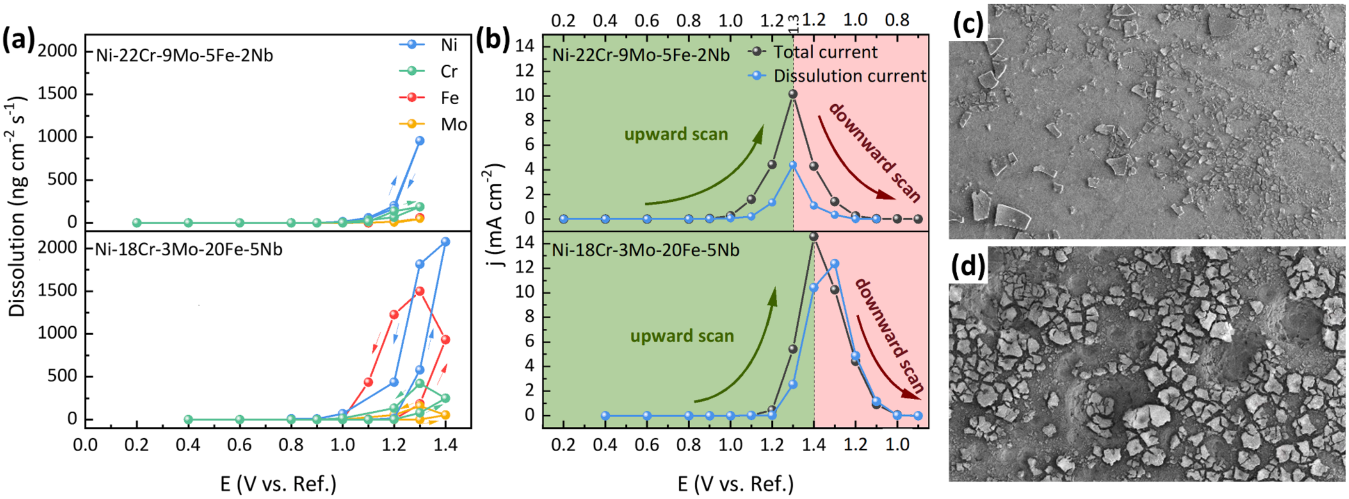

Fig. 7. (a) Dissolution rates for Ni, Cr, Fe, and Mo detected by in-situ XRF. (b) Comparison of measured total current density and dissolution current density calculated from XRF data. (c)-(d) SEM images of Ni-22Cr-9Mo-5Fe-2Nb and Ni-18Cr-3Mo-20Fe-5Nb, respectively, after the entire upward and downward potential steps.

bulk material. In this case, a higher proportion of Mo in the subsurface alloy layer is found by APXPS analysis (Fig. 2f), which explains the higher density of the subsurface alloy layer (Fig. 3b).

After the onset of passivity breakdown, the concentration of V_M is increased due to enhanced metal dissolution. The density of the subsurface alloy layer of Ni-22Cr-9Mo-5Fe-2Nb decreased from 8.9 to 8.1 g/cm^3 from 0.8 to 0.9 V (Fig. 3b), corresponding to the generation of 10 % vacancies, which are mainly Ni vacancies (V_{Ni}) since the dissolution of Cr, Mo, Fe, and Nb is negligible up to 1.0 V (Fig. 7a). In the transpassive potential range between 0.9 and 1.3 V, the OER occurs and corrosion products forms, so surface sensitive APXPS and XRR could not be measured, whereas GI-XRD still could be used to detect the change of

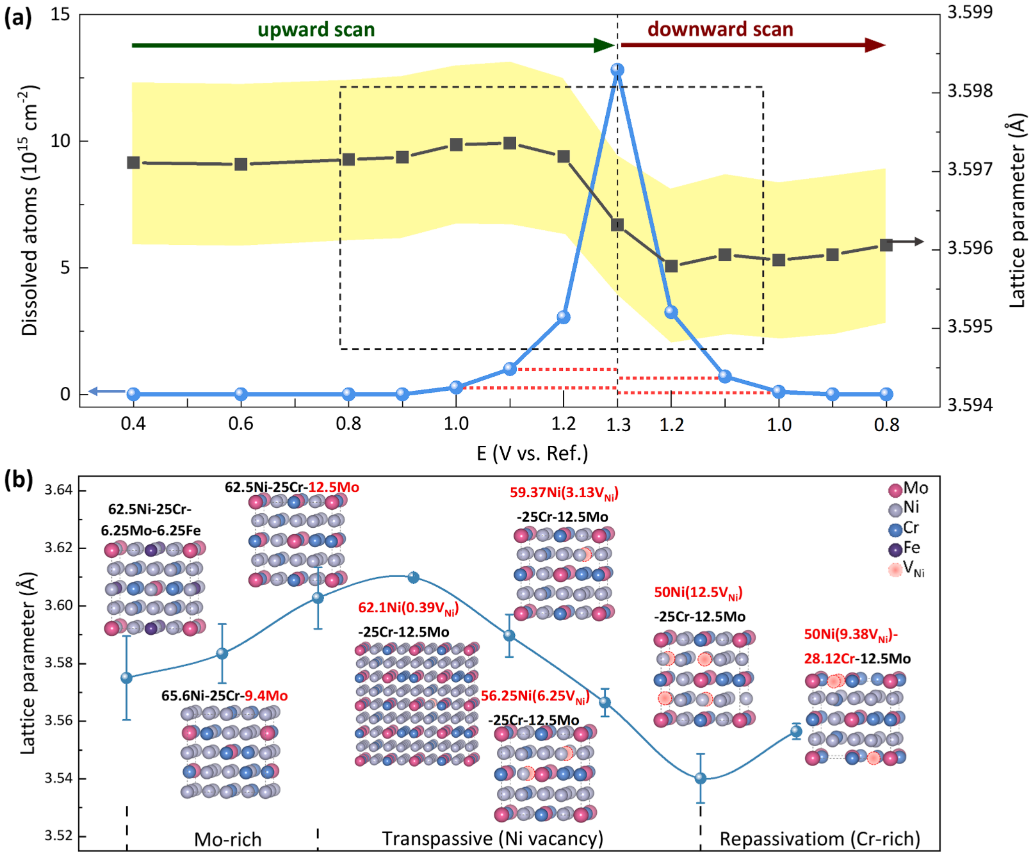

Fig. 8. (a) GI-XRD results showing evolution of lattice parameter (filled black squares) of the subsurface alloy layer for Ni-22Cr-9Mo-5Fe-2Nb along with the applied potential. The changes of dissolved metal atoms (filled blue circles) detected by XRF are also included in (a). Red dot lines compare the dissolution rate between downward steps and upward steps with the same applied potential. (b) DFT calculations of lattice parameter of the subsurface alloy layer along with composition changes and vacancy generation according to conditions in the dash box in (a). Error bars represent standard deviation of different configurations with various vacancy positions.

lattice parameter of the subsurface alloy layer. The incident angle of X-ray beam was 0.3° so that the penetration depth covers the subsurface alloy layer. Fig. 8a shows the evolution of the lattice parameter (right-axis) with the applied potential, plotted together with the dissolved metal atoms per unit surface area (left-axis) calculated by integration of the instant dissolved metal ion concentration in the electrolyte (XRF results) over time at each applied potential. The highlighted band region of the lattice parameter refers to the different crystal planes, which shows the same evolution trend. It can be seen that the lattice parameter increased significantly with the increased potential between 0.9 and 1.0 V due to the onset of active dissolution, which could be related to the enrichment of Mo in the subsurface alloy layer (Fig. 2f). The DFT calculations for the subsurface alloy layer with different compositions focus on the dashed box in Fig. 8a, further proving the possible enrichment of Mo (larger atomic radius) leads to the increase of lattice parameter for the subsurface alloy layer below 1.1 V, which is shown as the Mo-rich region in Fig. 8b. The plotted values and error bars represent the average lattice parameter and the mean square error between different arrangements of the computation models (examples are shown in Fig. 8b). More calculation details are given in Supplementary Note 6.

After pronounced dissolution occurred around 1.0 V, the lattice parameter of the subsurface alloy layer for Ni-22Cr-9Mo-5Fe-2Nb firstly increased slightly from 1.0 to 1.1 V, then sharply decreased from 1.1 to 1.3 V due to the greatly enhanced metal dissolution. Subsequently, the lattice of the subsurface alloy layer remains in the contracted state as the applied potential decreased in the downward steps. The sample after the measurement shows a flat surface without sign of localized corrosion, confirming a repassivation by the action of hidden subsurface alloy layer along by contracting the lattice. To understand the repassivation process by the role of hidden subsurface alloy layer, we performed DFT calculations of severe anodic dissolution by inducing vacancies within a supercell containing 62.5 at% Ni, 25 at% Cr, and 12.5 at% Mo, which is the composition similar to the subsurface alloy layer at 0.9 V. The key results are presented as the Ni dissolution region in Fig. 8b. Other simulation details can be found in Supplementary Note 6.

For Ni-22Cr-9Mo-5Fe-2Nb, Ni dissolution is dominant in the corrosion process after passivity breakdown (Fig. 7a), which leads to the formation of Ni vacancies in the subsurface alloy layer. It is shown in Fig. 8b that 0.39 % Ni vacancy results in the lattice expansion, in agreement with the GI-XRD results obtained from 1.0 to 1.1 V. The lattice expansion weakens the interactions between atoms, which further promotes the diffusion of metal atoms through the vacancies thus facilitating dissolution and generation of more vacancies. The highly defective crystals contract, leading to a decrease in lattice parameter when the vacancy density increases, e.g., to 3.13 % or above, which is consistent with the significant lattice contraction from 1.1 to 1.3 V according to the GI-XRD results.

The formation of a corrosion product layer (Supplementary Note 5) also confirms an enhanced dissolution of the subsurface alloy layer. The presence of Fe-, Mo-, and Nb-compounds in the corrosion product layer indicates possible generation of Fe, Mo, and Nb vacancies in the subsurface alloy layer. However, their contents in the alloy are much lower than Ni, so their vacancies are much less and their effects are not assessed here.

Accompanied by the increase in vacancies induced by metal dissolution, the outward diffusion of metal atoms is also promoted by the vacancies. As the applied potential decreases in the downward steps, the vacancy formation and occupation rates reach a balanced state, which is followed by a dominant occupation of vacancies as the metal dissolution rate further decreases. The XRF results reveal that the base metal Ni is dominant in the dissolution. Fe is also selectively dissolved, which is detected for Ni-18Cr-3Mo-20Fe-5Nb with a high Fe content. The alloying element Mo gets enriched in the subsurface alloy layer and also oxidized to form high valence compounds in the passive film (APXPS results), which may partially dissolve at high potentials (XRF results) and form precipitated corrosion products (SEM/EDS results). This implies that Cr is further enriched in the subsurface alloy layer due to the minor consumption (XRF results) during the transpassive dissolution. In order to understand the role of Cr in the subsurface alloy layer in the transpassive-repassivation process, the DFT calculated dissolution activation energies [44] are compared between pure Ni and Ni-25 %Cr, Ni-25 %Mo, and Ni-25 %Fe binary systems (Fig. 9a). The Ni-Cr system has higher dissolution energy compared with the Ni-Ni, Ni-Fe, and Ni-Mo systems, which indicates that the solution of Cr element will suppress the dissolution rate of Ni. Moreover, the dissolution activation energy increases when more Cr atoms solute in to the Ni matrix. According to the ELF analysis in Fig. 9b, the Ni-Cr bond is metal bond, whose strength will be enhanced by the increase of Cr. This explains that, with the enrichment of Cr in the subsurface alloy layer, the dissolution rate of Ni becomes lower during the repassivation process (downward steps), compared to the transpassive dissolution process (upward steps) with the same applied potential, which are marked as red dot lines in Fig. 8a.

In addition, there is a slightly increasing trend in the lattice parameter of the subsurface alloy layer during the downward potential steps below 1.2 V. This is likely due to filling of the vacancies by metal atoms from the bulk. Since Cr is enriched in the subsurface alloy layer, and Ni atom in Ni-Cr bond requires the highest energy to dissolve, the Cr atoms are expected to fill nickel vacancies, forming strong Cr-Ni bonds with surrounding Ni atoms, which also expand the lattice as shown in the repassivation region in Fig. 8b. The strengthened Cr-Ni bonds was proposed to be related to a difference in electro-negativity between adjacent Cr and Ni atoms, which adds partial ionic connection to the metal bonds [43]. This is also seen in our simulated subsurface alloy layer with Cr enrichment; therefore, a higher energy is required to release the Ni atoms from the subsurface alloy layer under the constraints by neighboring Cr atoms.

Fig. 10 is a schematic diagram illustrating the 'transpassive-repassivation' mechanism by the action of the subsurface alloy layer for the Ni-base super alloys with a low Fe content, including the processes occurring from passivity breakdown to repassivation. After the onset of passivity breakdown, degradation of the passive film takes place, accompanied by the Mo enrichment in the subsurface alloy layer. Then, enhanced Ni dissolution occurs at high anodic potentials, leading to Cr enrichment in the subsurface alloy layer. When the applied potential is decreased, the repassivation process occurs because of the Cr enrichment in the subsurface alloy layer that strengthen the metal bonds. The reinforced strength of the Cr-Ni bonds raises the dissolution activation energy and suppresses further metal dissolution. When the applied potential is decreased to a certain level, the alloy regains a passive state, i.e., repassivation, which is favored by the Cr-rich subsurface alloy layer. Additionally, the formation of stable Nb oxide in the passive film is also beneficial for the repassivation. On the other hand, Fe as another main alloying element, does not seem to possess the repassivation ability because of a lower bond strength and a lower dissolution activation energy of Fe-Ni compared with Cr-Ni system, thus explaining the lower ability for repassivation of the high Fe-content Ni alloy in this study (Ni-18Cr-3Mo-20Fe-5Nb).

4. Conclusion

The combined synchrotron experiments and first principles modelling in this work provide an atomistic understanding of the repassivation mechanism of Ni-base superalloys regarding the role of the main alloying elements in the formation of the passive film, transpassive dissolution, and repassivation process. The multimodal in-situ synchrotron X-ray measurements provide unprecedent information of the whole interfacial region from the electrolyte, through the passive film, to the subsurface alloy layer. The DFT calculations yield energetics of ionic transport in highly defective oxides, as well as the changes in lattice parameters in the subsurface alloy layer. Following conclusions can be drawn:

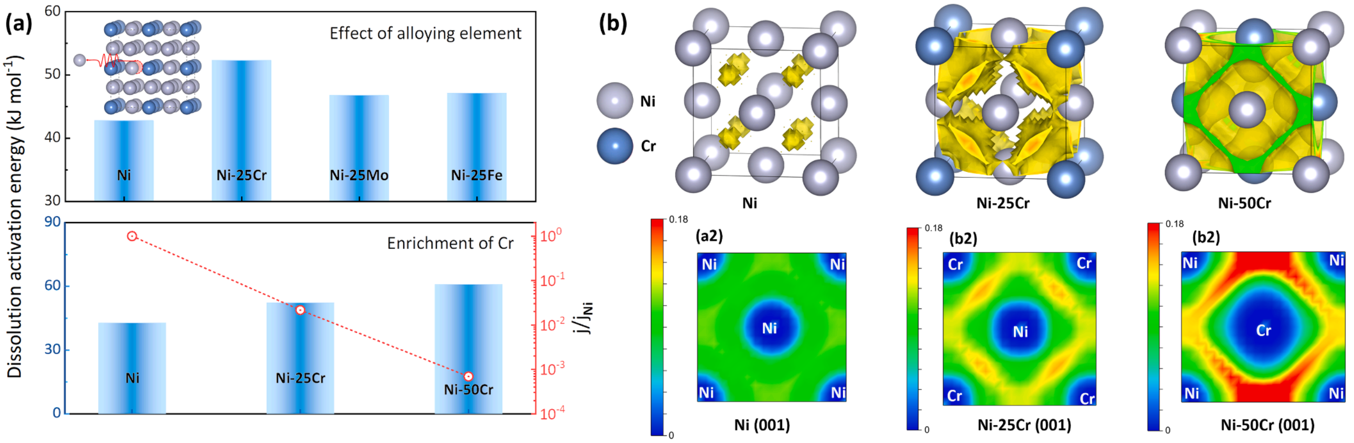

Fig. 9. (a) Effect of alloying elements (Fe, Cr, and Mo) at 25 at% level and effect of the Cr concentration in Cr-Ni alloy on the computational dissolution activation energy for Ni releasing from the subsurface alloy layer. j/j_{Ni} is the dissolution rate ratio of Ni-xCr to Ni. (b) Electron localization function (ELF) analysis of Ni, Ni-25Cr and Ni-50Cr, where all isosurfaces are set as 0.13.

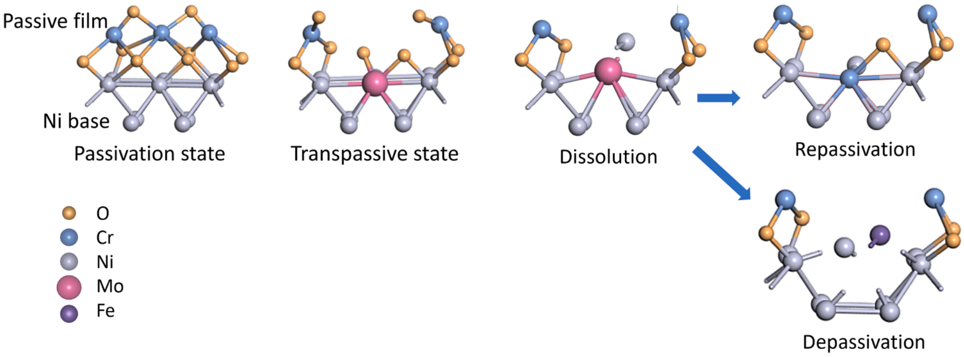

Fig. 10. Schematic diagram of transpassive-repassivation process by the action of subsurface layer of Ni-base superalloy with a low Fe content. The gray, orange, blue, pink, and purple ball-sticks represent Ni, O, Cr, Mo, and Fe atoms and the bonds between them, respectively.

In passive condition, Cr^{3+} oxide is enriched and multi-valence Mo and Nb species are present in the passive film, while Cr^{3+} hydroxide is present on top of the passive film. With increasing potential, the oxide layer grows slightly, the low-valence Mo and Nb species are oxidized to high-valence Mo and Nb compounds. The oxide thickens and Mo becomes enriched in the subsurface alloy layer at the potential near transpassive breakdown.

After the onset of transpassive breakdown, the oxide film becomes highly defective with high density of cation vacancies leading to largely enhanced the metal dissolution. The dissolving metal is mostly Ni for Ni-22Cr-9Mo-5Fe-2Nb (lower Fe-content and higher Mo-content), but both Ni and Fe are dissolving from Ni-18Cr-3Mo-20Fe-5Nb (higher Fe-content and lower Cr- and Mo-contents). Dissolution of Cr and Mo also occurs at a low rate, more from Ni-18Cr-3Mo-20Fe-5Nb than Ni-22Cr-9Mo-5Fe-2Nb, while Nb forms stable oxide that remain in the passive film or adherent corrosion products. The metal dissolution is accelerated at high potentials, which generate a high density of Ni vacancy and relative enrichment of Cr in the subsurface layer.

When the applied potential is decreased from the high value, Ni-22Cr-9Mo-5Fe-2Nb has a stronger ability for repassivation than Ni-18Cr-3Mo-20Fe-5Nb. The highly defective passive film does not act as an effective barrier, while the subsurface alloy layer plays an important role in the repassivation process. The Cr enrichment and high density of Ni vacancy in the subsurface alloy layer gives Ni-22Cr-9Mo-5Fe-2Nb (with a low Fe content) a favorable repassivation property, by enhanced outward Cr diffusion to increase the Cr-Ni bonds impeding metal dissolutionand to repair the defective passive film, leading to repassivation when the high potential is removed. This mechanism by strengthening the Cr-Ni bonds is not operative for Fe-rich alloys.

The role of the subsurface alloy layer needs to be considered for the understanding of the passivity and ability for repassivation of advanced alloys. The new knowledge gained in this work also provides guidelines for the design of high-performance corrosion resistant alloys.

CRediT authorship contribution statement

Ulrich Lienert: Supervision, Methodology. **Zoltan Hegedüs:** Methodology, Investigation. **Andrea Grespi:** Investigation. **Grespi Giuseppe:** Investigation. **Arno Jeromin:** Investigation. **Keller Thomas F:** Supervision, Resources. **Mattia Scardamaglia:** Methodology, Investigation. **Edvin Lundgren:** Supervision, Methodology, Investigation. **Alfred Larsson:** Writing – review & editing, Visualization, Software, Methodology, Investigation, Formal analysis, Data curation. **Jinshan Pan:** Writing – review & editing, Validation, Supervision, Resources, Project administration, Methodology, Investigation, Funding acquisition, Conceptualization. **Dihao Chen:** Writing – review & editing, Writing – original draft, Validation, Software, Methodology, Investigation, Formal analysis, Data curation, Conceptualization. **Andrey Shavorskiy:** Supervision, Resources, Methodology. **Chaofang Dong:** Supervision, Resources, Methodology. **Xiaoqi Yue:** Writing – review & editing, Writing – original draft, Visualization, Validation, Methodology, Investigation, Formal analysis, Data curation, Conceptualization.

Declaration of generative AI and AI-assisted technologies in the writing process

We have not used any AI tool in the preparation and revision processes of this manuscript.

Declaration of Competing Interest

The authors declare the following financial interests/personal relationships which may be considered as potential competing interests: Jinshan Pan reports that financial supports for this work were provided by Swedish Foundation for Strategic Research and Swedish Research Council. The other authors declare that they have no known competing financial interests or personal relationships that could have appeared to influence the work reported in this paper.

Acknowledgements

This work was financially supported by Swedish Foundation for Strategic Research (SSF project no. ID19–0032) and Swedish Research Council (project numbers 2021–04157, 2020–06154 and 2018–03434). We thank Josefin Eidhagen at Alleima AB for preparing the samples. D. C. gratefully acknowledges the China Scholarship Council for supporting his stay at KTH Royal Institute of Technology, Sweden. We acknowledge DESY (Hamburg, Germany), a member of the Helmholtz Association HGF, for the provision of experimental facilities. Parts of this research were carried out at the PETRA III beamline P21.2. Beamtime at DESY was allocated for the proposal II-20190755 EC and I-20211350 EC. We also thank MAX IV Laboratory for the access to HIPPIE Beamline under Proposal 20210831. Research conducted at MAX IV, a Swedish national user facility, is supported by the Swedish Research council under contract 2018–07152, the Swedish Governmental Agency for Innovation Systems under contract 2018–04969, and Formas under contract 2019–02496. Moreover, we acknowledge the National Academic Infrastructure for Supercomputing in Sweden (NAISS) partially funded by the Swedish Research Council through grant agreement no. 2022–06725 for awarding this project access to the LUMI supercomputer, owned by the EuroHPC Joint Undertaking, hosted by CSC (Finland) and the LUMI consortium.

Appendix A. Supporting information

Supplementary data associated with this article can be found in the online version at doi:10.1016/j.corsci.2025.113321.

Data availability

Data will be made available on request.

References

[1] U.R. Evans, Passivity and protective oxide films, Nature 121 (1928) 351–352, https://doi.org/10.1038/121351b0.

[2] D.D. Macdonald, Passivity–the key to our metals-based civilization, Pure Appl. Chem. 71 (1999) 951–978.

[3] J. Soltis, Passivity breakdown, pit initiation and propagation of pits in metallic materials–review, Corros. Sci. 90 (2015) 5–22, https://doi.org/10.1016/j.corsci.2014.10.006.

[4] G. Frankel, Pitting corrosion of metals: a review of the critical factors, J. Electrochem. Soc. 145 (1998) 2186, https://doi.org/10.1149/1.1838615.

[5] S. Zhang, H. Feng, H. Li, Z. Jiang, T. Zhang, H. Zhu, Y. Lin, W. Zhang, G. Li, Design for improving corrosion resistance of duplex stainless steels by wrapping inclusions with niobium armour, Nat. Commun. 14 (2023) 7869, https://doi.org/10.1038/s41467-023-43752-8.

[6] P. Marcus, On some fundamental factors in the effect of alloying elements on passivation of alloys, Corros. Sci. 36 (1994) 2155–2158, https://doi.org/10.1016/0010-938X(94)90013-2.

[7] Y. Xie, D.M. Artymowicz, P.P. Lopes, A. Aiello, D. Wang, J.L. Hart, E. Anber, M. L. Taheri, H. Zhuang, R.C. Newman, Others, a percolation theory for designing corrosion-resistant alloys, Nat. Mater. 20 (2021) 789–793, https://doi.org/10.1038/s41563-021-00920-9.

[8] H.-H. Strehblow, V. Maurice, P. Marcus, Corrosion mechanisms in theory and practice, CRC press, Taylor & Francis Group, 2012.

[9] A. Bandyopadhyay, K.D. Traxel, M. Lang, M. Juhasz, N. Eliaz, S. Bose, Alloy design via additive manufacturing: advantages, challenges, applications and perspectives, Mater. Today 52 (2022) 207–224, https://doi.org/10.1016/j.mattod.2021.11.026.

[10] J. Eidhagen, A. Larsson, A. Preobrajenski, A. Delblanc, E. Lundgren, J. Pan, Synchrotron XPS and electrochemical study of aging effect on passive film of ni alloys, J. Electrochem. Soc. 170 (2023) 021506, https://doi.org/10.1149/1945-7111/acba4b.

[11] A. Larsson, G. D'Acunto, M. Vorobyova, G. Abbondanza, U. Lienert, Z. Hegedüs, A. Preobrajenski, L.R. Merte, J. Eidhagen, A. Delblanc, et al., Thickness and composition of native oxides and near-surface regions of ni superalloys, J. Alloy. Compd. 895 (2022) 162657, https://doi.org/10.1016/j.jallcom.2021.162657.

[12] E. Sikora, D.D. Macdonald, Nature of the passive film on nickel, Electrochim. Acta 48 (2002) 69–77, https://doi.org/10.1016/S0013-4686(02)00552-2.

[13] B. Lynch, S. Neupane, F. Wiame, A. Seyeux, V. Maurice, P. Marcus, An XPS and ToF-SIMS study of the passive film formed on a model FeCrNiMo stainless steel surface in aqueous media after thermal pre-oxidation at ultra-low oxygen pressure, Appl. Surf. Sci. 554 (2021) 149435, https://doi.org/10.1016/j.apsusc.2021.149435.

[14] X. Li, K. Ogle, The passivation of Ni-Cr-Mo alloys: time resolved enrichment and dissolution of cr and mo during passive-active cycles, J. Electrochem. Soc. 166 (2019) C3179, https://doi.org/10.1149/2.0201911jes.

[15] C.-O. Olsson, D. Landolt, Atmospheric oxidation of a Nb–Zr alloy studied with XPS, Corros. Sci. 46 (2004) 213–224, https://doi.org/10.1016/S0010-938X(03)00139-2.

[16] H. Hardy, A "sub-regular" solution model and its application to some binary alloy systems, Acta Metall. 1 (1953) 202–209, https://doi.org/10.1016/0001-6160(53)90059-5.

[17] G.T. Burstein, P.I. Marshall, The coupled kinetics of film growth and dissolution of stainless steel repassivating in acid solutions, Corros. Sci. 15 (1984) 449–462, https://doi.org/10.1016/0010-938X(84)90070-2.

[18] G.S. Frankel, N. Sridhar, Understanding localized corrosion, Mater. Today 11 (2008) 38–44, https://doi.org/10.1016/S1369-7021(08)70206-2.

[19] Y. Hua, S. Shi, H. Wang, L. Wang, X. Yue, C. Su, Insight into surface microstructure evolution and fracture mechanism of incoloy alloy 800HT under high-temperature conditions, J. Mater. Res. Technol. (2025), https://doi.org/10.1016/j.jmrt.2025.02.138.

[20] A. Larsson, A. Grespi, G. Abbondanza, J. Eidhagen, D. Gajdek, K. Simonov, X. Yue, U. Lienert, Z. Hegedüs, A. Jeromin, et al., The oxygen evolution reaction drives passivity breakdown for Ni–Cr–Mo alloys, Adv. Mater. (2023) 2304621, https://doi.org/10.1002/adma.202304621.

[21] J.D. Henderson, X. Li, D.W. Shoesmith, J.J. Noël, K. Ogle, Molybdenum surface enrichment and release during transpassive dissolution of Ni-based alloys, Corros. Sci. 147 (2019) 32–40, https://doi.org/10.1016/j.corsci.2018.11.005.

[22] A. Mishra, D. Shoesmith, The activation/depassivation of nickel–chromium–molybdenum alloys: an oxyanion or a ph effect—Part II, Electrochim. Acta 102 (2013) 328–335, https://doi.org/10.1016/j.electacta.2013.03.177.

[23] J.D. Henderson, X. Li, F.P. Filice, D. Zagidulin, M.C. Biesinger, B. Kobe, D. W. Shoesmith, K. Ogle, J.J. Noël, Investigating the role of mo and cr during the activation and passivation of Ni-based alloys in acidic chloride solution, J. Electrochem. Soc. 168 (2021) 021509, https://doi.org/10.1149/1945-7111/abe47a.

[24] B. Zhang, J. Wang, B. Wu, X. Guo, Y. Wang, D. Chen, Y. Zhang, K. Du, E. Oguzie, X. Ma, Unmasking chloride attack on the passive film of metals, Nat. Commun. 9 (2018) 2559, https://doi.org/10.1038/s41467-018-04942-x.

[25] J.W. Oldfield, Test techniques for pitting and crevice corrosion resistance of stainless steels and nickel-base alloys in chloride-containing environments, Int. Mater. Rev. 32 (1987) 153–172, https://doi.org/10.1179/095066087790150313.

[26] T. Li, J. Wu, G. Frankel, Localized corrosion: passive film breakdown vs. Pit growth stability, part VI: pit dissolution kinetics of different alloys and a model for pitting and repassivation potentials, Corros. Sci. 182 (2021) 109277, https://doi.org/10.1016/j.corsci.2021.109277.

[27] S. Zhang, Y. Wang, S. Li, Z. Wang, H. Chen, L. Yi, X. Chen, Q. Yang, W. Xu, A. Wang, et al., Concerning the stability of seawater electrolysis: a corrosion mechanism study of halide on Ni-based anode, Nat. Commun. 14 (2023) 4822, https://doi.org/10.1038/s41467-023-40563-9.

[28] A. Doroudi, A. Dastgheib, H. Omidvar, The bonding temperature effect of the diffusion brazing inconel 625 superalloy on the microstructure changes, corrosion resistance, and mechanical properties, J. Manuf. Process. 53 (2020) 213–222, https://doi.org/10.1016/j.jmapro.2020.02.005.

[29] A. Mishra, D. Richesin, R.B. Rebak, Localized corrosion study of Ni-Cr-Mo alloys for oil and gas applications, in: NACE CORROSION, NACE, 2015. : p. NACE-2015.

[30] G. Wood, T. Hodgkiess, Mechanism of oxidation of dilute nickel–chromium alloys, Nature 211 (1966) 1358–1361, https://doi.org/10.1038/2111358a0.

[31] X. Wei, B. Zhang, B. Wu, Y. Wang, X. Tian, L. Yang, E. Oguzie, X. Ma, Enhanced corrosion resistance by engineering crystallography on metals, Nat. Commun. 13 (2022) 726, https://doi.org/10.1038/s41467-022-28368-8.

[32] S. Zhu, M. Scardamaglia, J. Kundsen, R. Sankari, H. Tarawneh, R. Temperton, L. Pickworth, F. Cavalca, C. Wang, H. Tissot, et al., HIPPIE: a new platform for ambient-pressure X-ray photoelectron spectroscopy at the MAX IV laboratory, J. Synchrotron Radiat. 28 (2021) 624–636, https://doi.org/10.1107/S160057752100103X.

[33] A. Larsson, K. Simonov, J. Eidhagen, A. Grespi, X. Yue, H. Tang, A. Delblanc, M. Scardamaglia, A. Shavorskiy, J. Pan, E. Lundgren, In situ quantitative analysis of electrochemical oxide film development on metal surfaces using ambient pressure X-ray photoelectron spectroscopy: industrial alloys, Appl. Surf. Sci. (2022) 155714, https://doi.org/10.1016/j.apsusc.2022.155714.

[34] M. Schmid, H.-P. Steinrück, J.M. Gottfried, A new asymmetric Pseudo-Voigt function for more efficient fitting of XPS lines, Surf. Interface Anal. 46 (2014) 505–511.

[35] X. Yue, A. Larsson, H. Tang, A. Grespi, M. Scardamaglia, A. Shavorskiy, A. Krishnan, E. Lundgren, J. Pan, Synchrotron-based near ambient-pressure X-ray photoelectron spectroscopy and electrochemical studies of passivation behavior of N-and V-containing martensitic stainless steel, Corros. Sci. 214 (2023) 111018, https://doi.org/10.1016/j.corsci.2023.111018.

[36] A. Stierle, T.F. Keller, H. Noei, V. Vonk, R. Roehlsberger, Desy nanolab, journal of Large-Scale research facilities, A76–A76, JLSRF 2 (2016), https://doi.org/10.17815/jlsrf-2-140.

[37] W. Kohn, L.J. Sham, Self-consistent equations including exchange and correlation effects, Phys. Rev. 140 (1965) A1133, https://doi.org/10.1103/PhysRev.140.A1133.

[38] J.P. Perdew, K. Burke, M. Ernzerhof, Generalized gradient approximation made simple, Phys. Rev. Lett. 77 (1996) 3865, https://doi.org/10.1103/PhysRevLett.77.3865.

[39] H.J. Monkhorst, J.D. Pack, Special points for Brillouin-zone integrations, Phys. Rev. B 13 (1976) 5188, https://doi.org/10.1103/PhysRevB.13.5188.

[40] G. Henkelman, B.P. Uberuaga, H. Jónsson, A climbing image nudged elastic band method for finding saddle points and minimum energy paths, J. Chem. Phys. 113 (2000) 9901–9904, https://doi.org/10.1063/1.1329672.

[41] A. Rohrbach, J. Hafner, G. Kresse, Ab initio study of the (0001) surfaces of hematite and chromia: influence of strong electronic correlations, Phys. Rev. B 70 (2004) 125426, https://doi.org/10.1103/PhysRevB.70.125426.

[42] Q. Zhou, C. Xu, J. Hou, W. Ma, T. Jian, S. Yan, H. Liu, Duplex interpenetrating-phase FeNiZn and FeNi3 heterostructure with low-gibbs free energy interface coupling for highly efficient overall water splitting, NanoMicro Lett. 15 (2023) 95, https://doi.org/10.1007/s40820-023-01066-w.

[43] H. Ke, C.D. Taylor, DFT-based calculation of dissolution activation energy and kinetics of Ni–Cr alloys, J. Electrochem. Soc. 167 (2020) 131508, https://doi.org/10.1149/1945-7111/abbbbd.

[44] D. Chen, W. Zhou, Y. Ji, C. Dong. Applications of density functional theory to corrosion and corrosion prevention of metals: A review. MGE Advances 3 (2025) e83, 1-59, doi: 10.1002/mgea.83.